Supplemental Material: Optimal protocols and universal time-energy bound in Brownian thermodynamics

Yoseline Rosales-Cabara,[1] Giovanni Manfredi,[2,*] Gabriel Schnoering,[1]
Paul-Antoine Hervieux,[2,†] Laurent Mertz,[3,‡] and Cyriaque Genet[1,§]

[1] *Université de Strasbourg, CNRS, Institut de Science et d'Ingénierie Supramoléculaires, UMR 7006, F-67000 Strasbourg, France*
[2] *Université de Strasbourg, CNRS, Institut de Physique et Chimie des Matériaux de Strasbourg, UMR 7504, F-67000 Strasbourg, France*
[3] *NYU-ECNU Institute of Mathematical Sciences at NYU Shanghai,, Shanghai, 200062, China*

(Dated: September 26, 2019)

A: SETUP, CALIBRATION, UNCERTAINTIES

Optical trap setup

All experiments are performed on single optically trapped polystyrene spheres (radius $R = 500$ nm) taken from a monodisperse ($\delta R/R = 0.028$) solution (ThermoFisher, FluoSpheres) and enclosed inside a fluidic cell filled with dionized water. The microfluidic cell is made with a microscope slide and a 170 μm thick glass coverslip, sealed with a 120 μm thick spacer.

The optical trap, described in details in Fig. 1, is an evolution of the setup described in our previous work [1]. It uses a CW near-infrared (λ_T =785 nm) laser whose intensity – hence the trap stiffness – can be modulated externally using a waveform generator. Any trapping protocol can then be implemented by computer-programming the waveform generator so that the time-evolution of the trap stiffness follows the desired profile.

Under such trapping laser modulation, the instantaneous axial motion $x(t)$ of the bead is monitored using an auxiliary laser propagating in the opposite direction of the trapping laser (see Fig. 1). We checked that this low-power probe beam, injected in the fluidic cell from its back-side, does not exerts any spurious optical force of the trapped bead. The signal collected by the photodiode and the output voltage of the waveform generator are simultaneously registered by a multichannel acquisition card (National Instruments, NI-6251) with a sampling rate $f_s = 262$ kHz. In order to span the signal in the full dynamic range of the acquisition card, the generator output voltage was re-scaled using a scaling amplifier (Stanford Research Systems, SIM983) and the voltage time series of the photodiode was amplified and filtered using low-noise pre-amplifiers (Stanford Research Systems, SR560).

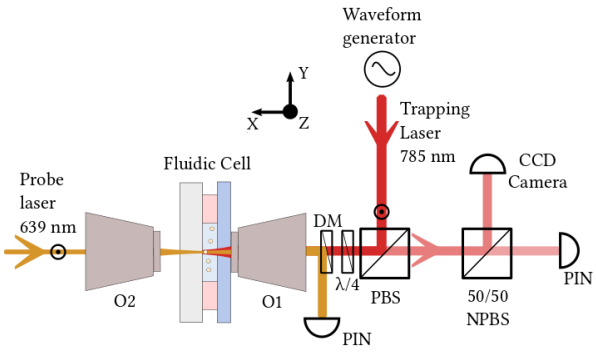

FIG. 1. The trapping laser ($\lambda_T = 785$ nm, 100 mW, TEM_{00}, CW, Coherent, OBIS LX785) is modulated externally using a waveform generator (Agilent, 33220A). Linearly polarized along the $z-$axis, the beam is sent to a water-immersion objective (O1, 100×, 1.2 numerical aperture (NA)) through a polarizing beam splitter (PBS) and a quarter-wave plate ($\lambda/4$). The intensity $I(t)$ partially reflected by the end-surface of the fluidic cell varies linearly with the displacement $x(t)$ of the polystyrene microsphere inside the trap. This intensity $I(t)$ is collected and recorded by a *p-i-n* photodiode (Thorlabs, DET10A), while a CCD camera is used in the other port of the non polarizing beam splitter (NPBS) for imaging. The probe beam consists of a second laser (639 nm, 70 mW Thorlabs laser diode, linearly polarized) of low power (400 μW). It is injected inside the trap collinearly with the trapping beam but from behind the fluidic cell using a dry objective (O2, 60×, NA 0.7). This second beam is separated from the trapping beam using a dichroic mirror (DM) and the interference between the transmitted beam and the diffracted light by the bead is recorded using a second *p-i-n* photodiode (Thorlabs, DET10A) placed in a plane conjugated to the back focal plane of the trapping objective. In order to ensure that a single bead is trapped without other beads in its vicinity, potentially perturbing the dynamics, the optical trap is equipped with an interferometric scattering microscope not shown here but described in details in our previous work [2].

Stiffness modulation calibration

The trapping laser is modulated according to a given protocol $\kappa(t)$, defined and calculated with chosen transition parameters $(\kappa_i, \kappa_f, \Delta t)$. In order to convert this protocol $\kappa(t)$ into a modulating voltage $V_{\rm mod}(t)$ for the waveform generator, a calibration procedure is performed. This procedure consists in measuring the trap stiffnesses associated with a series of consecutive values of DC voltages, i.e. consecutive trapping laser intensities. Each stiffness is extracted from a Lorentzian fit of the corresponding motional power spectral density (PSD) of the trapped bead. Associated error bars are obtained from the uncertainties of the Lorentzian fits (MATLAB Levenberg-Marquardt algorithm). The calibration curve shown in Fig. 2 corresponds to a linear fit of the evolution of such measured stiffnesses (including their error bars) as a function of the DC voltages.

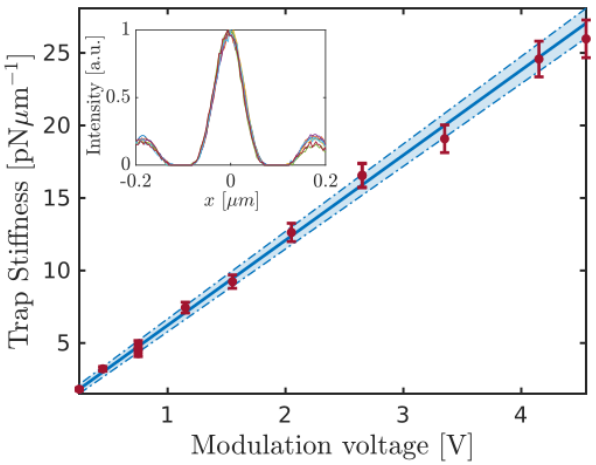

FIG. 2. Evolution of the trap stiffnesses as a function of DC waveform generator voltages. The red dots represent the stiffness values extracted from the motional PSD, with error bars for each point combining the uncertainties of the Lorentzian fit of each PSD and the error made on the Stokes drag $\gamma = 6\pi R\eta$ due to the polystyrene sphere radius dispersion $\delta R/R$. The solid line is the linear fit and the shaded area represents a 95 % confidence interval for the estimated linear regression parameters taking into account the weights of the data points. The (normalized) evolution of the trapping beam profile at the waist inside the trap is displayed in the inset through a ramping of the modulation voltage, corresponding to successive trapping laser intensities. These measurements demonstrate the stability of the trapping laser profile at the waist throughout intensity modulation protocols.

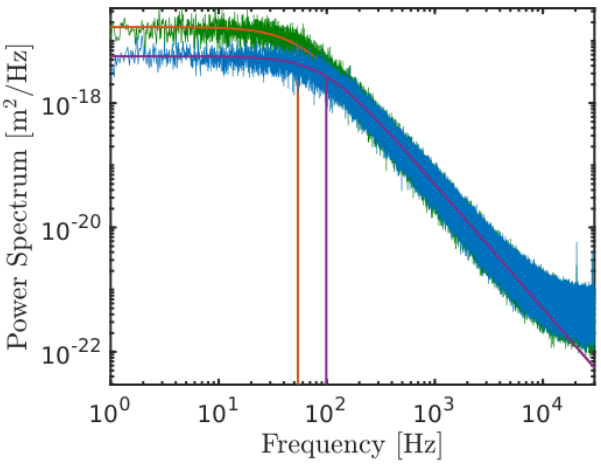

FIG. 3. Power spectral density of the concatenated trajectories corresponding to the sections of the cycles for which κ is fixed to κ_i is displayed in greeen. The best-fitted roll-off frequency $f_c = 52.63 \pm 0.01$ Hz (vertical red line) yields $\kappa_i = 2.78 \pm 0.08$ pN/μm, and the position sensitivity parameter is $\beta = \sqrt{k_B T/\gamma D_{fit}} = 1.21 \pm 0.02$ μm/V -see below. The blue curve is the power spectral density of the concatenated trajectories corresponding to the sections of the cycles for which κ is fixed to κ_f. The best-fitted roll-off frequency is $f_c = 98.98 \pm 0.02$ Hz (vertical purple line) gives $\kappa_f = 5.22 \pm 0.15$ pN/μmfor this case. Here, the positional calibration factor is $\beta = 1.31 \pm 0.02$ μm/V. Lorentzian fits (continuous red and purple lines superimposed to the PSDs) are calculated by implementing a MATLAB Levenberg-Marquardt algorithm for non-linear leasts squares.

Monitoring Brownian dynamics

The time evolution of the Brownian system is monitored by recording the stochastic trajectory of the trapped bead over 2×10^4 cycles of the protocol $\kappa(t)$. Each cycle lasts 50 ms, where the first 30 ms correspond to the initial thermal equilibrium with κ_i and the remaining $(20 - \Delta t)$ ms correspond to the final thermal equilibrium at κ_f. Each stationary region of the full trajectory, i.e. corresponding to a constant κ (κ_i or κ_f), is sectioned and concatenated with all the other sliced trajectories under the same stiffness. The PSD of this concatenated trajectory is computed and a Lorentzian fit yields the ensemble average κ. Figs. 3 (a) and (b) respectively show the PSD of the concatenated trajectories for the equilibria κ_i and κ_f for the case $\Delta t \sim \tau_{\text{relax}}/10$ described in the main text.

Implementing the same procedure, the full temporal trace of the particle positions undergoing 2×10^4 cycles is chopped into trajectories that correspond to a single cycle of the protocol $\kappa(t)$. The ensemble of traces then consists of all the sub-trajectories superimposed within the same time interval, in such a way that they all start $t = -30$ ms with κ_i, as displayed in Fig. 4 below.

The instantaneous ensemble variance $s(t_j)$ at a time $t = t_j$ ($j = 1, \cdots, T \times f_s$), with $T = 50$ ms and $f_s = 2^{18}$ Hz) is obtained by a vertical cross-cut of the ensemble of trajectories plotted in Fig. 4. The resulting distribution of positions $\rho(x, t_j)$ is a Gaussian of zero mean $\mu_x(t_j)$ and variance $s(t_j)$. Fig. 5 displays the position distribution functions (PDF) before (equilibrium at κ_i) and after (equilibrium at κ_f) the change in trapping stiffness imposed by the protocol $\kappa(t)$. The corresponding trapping potentials calculated as $U(x, t_j) = -k_B T \log(\rho(x, t_j)) + \text{cst}$ are also shown and compared to the expected harmonic profiles $U = \frac{1}{2}\kappa x^2$ evaluated from the stiffnesses κ_i, κ_f that were extracted from the measured PSD shown in Fig 3.

Proceeding in the same manner but for all times t_j, we can obtain the temporal evolution of the ensemble variance $s(t)$ over the full protocol $\kappa(t)$. Note here that Figs. **??** are built from the same data collected during the same protocol of duration $\Delta t = 3.47 \times 10^{-4}$s.

From Brownian positions to variances

We remind here a classical result of correlation in the Langevin theory of overdamped Brownian motion -see for instance [3]. Starting from the Brownian positions $x(t)$ of the trapped particle that evolve according the overdamped Langevin equation

$$\gamma \frac{dx(t)}{dt} = -\kappa x(t) + F_{\text{th}}(t), \tag{1}$$

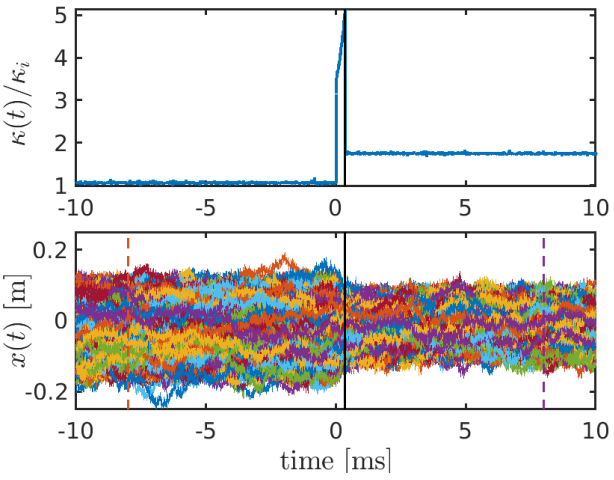

FIG. 4. Ensemble of trajectories corresponding to one cycle. Top: A single cycle of the control parameter $\kappa(t)$ normalized to κ_i. Bottom: Position fluctuations of the bead in the trap of modulated stiffness. The solid vertical lines indicate $\Delta t = 3.47 \times 10^{-4}$s. The position distribution functions calculated at the two times indicated by the dashed vertical lines in the lower panel are displayed in Fig. 5 below (top panel).

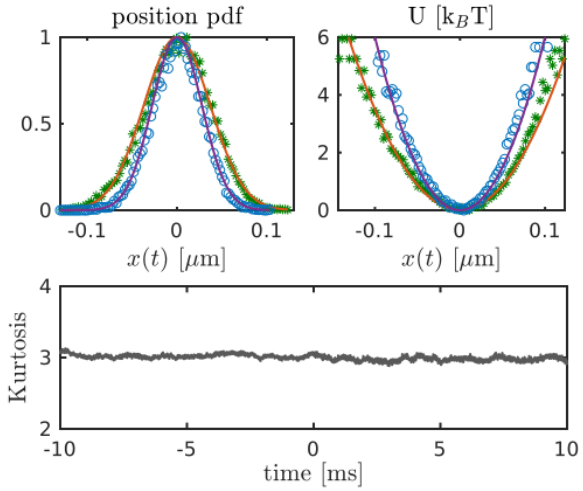

FIG. 5. Top-left panel: Position distribution functions (PDF) built from the ensemble of trajectories at the two different times $t_j < t_0$ and $t_j > t_f$ indicated by the two dashed vertical lines in Fig. 4 above (bottom panel), with associated trap stiffnesses κ_i and κ_f respectively. Top-right panel: Associated trapping potentials extracted from the PDF as $U(x,t_j) = -k_B T \log(\rho(x,t_j)) + \text{cst}$. The solid lines correspond to $U = \frac{1}{2}\kappa x^2$ with $\kappa = \kappa_i$ and $\kappa = \kappa_f$ extracted from the PSD shown in Fig. 3. Bottom panel: Kurtosis of each PDF for all times t_j.

where $\gamma = 6\pi R\eta$ is the Stokes drag coefficient, which depends on the radius of the particle $R = 500$ nm and the dynamic viscosity of the fluid $\eta \sim 10^{-3}$ Pa s at room temperature, and $D = k_B T/\gamma \sim 0.4\ \mu\text{m}^2/\text{s}$ the Brownian diffusion coefficient fixed by the temperature T of water (room temperature) and the Boltzmann constant k_B and $F_{\text{th}}(t) = \sqrt{2k_B T\gamma}\xi(t)$ is the stochastic Langevin force modeled with a Wiener process with $\langle \xi(t) \rangle = 0$ and $\langle \xi(t)\xi(t') \rangle = \delta(t-t')$, where $\langle \cdots \rangle$ stands for an ensemble average performed over all the realizations of the stochastic process.

Considering an initial position x_0, the solution of Eq. (1) writes as:

$$x(t) = x_0\, e^{-\kappa t/\gamma} + \frac{1}{\gamma}\int_0^t d\tau\, F_{\text{th}}(\tau)\, e^{\kappa(\tau-t)/\gamma}. \qquad (2)$$

The dynamical equation for the variance $s(t) = \langle x(t)^2 \rangle$ is obtained by multiplying both sides of Eq. (1) by $x(t)$ and by taking the ensemble average. This operation points to determining the correlation $\langle x(t)F_{\text{th}}(t) \rangle$ calculated with a (Stratonovich) stochastic integral as [4]

$$\langle x(t)F_{\text{th}}(t) \rangle = k_B T, \qquad (3)$$

from which the dynamical equation for the variance is simply given:

$$\gamma\frac{ds(t)}{dt} = -2\kappa s(t) + 2D\gamma. \qquad (4)$$

Normality tests

To confirm that all PDF remain Gaussian for all times, we calculate their kurtosis and verify, for the same $\Delta t = 3.47 \times 10^{-4}$s protocol -see Fig. 5, bottom panel- that all-time kurtosis remains very close to 3 throughout the entire protocol. This test is more critical for the shortest protocol of duration $\Delta t = 1.22 \times 10^{-4}$s which is shown in Fig. 6, upper panel. As seen in the lower panel, the kurtosis remains here too very close to 3 throughout the entire protocol. We supplement this kurtosis-based test of normality by showing the normalized PDF constructed from all positions recorded at different t_0, t_1, t_2 times within the protocols, t_0, t_1, t_2 and at thermal equilibrium t_4 after the $\Delta t = 1.22 \times 10^{-4}$s protocol. These selected times are shown as vertical lines in Fig. 6. As clearly seen in Fig. 7, the PDF can be well fitted by zero mean Gaussian distribution -with larger deviations on the PDf tails due to a reduction in statistics. Finally, in order to further assess the normal character of our PDF, we draw in Fig. 8 a quantile-quantile diagram that clearly show the expected proximity of our experimental PDF with a normal law. This diagrammatic analysis is also performed within the protocol -see inset of Fig. 8.

Statistical uncertainties

The uncertainties for the instantaneous ensemble variances are obtained following a χ^2 law with $N-1$ degrees of freedom where $N = N_{cycles}$ is the number of independent trajectories $x_i(t)$ undergoing one cycle of the protocol $\kappa(t)$.

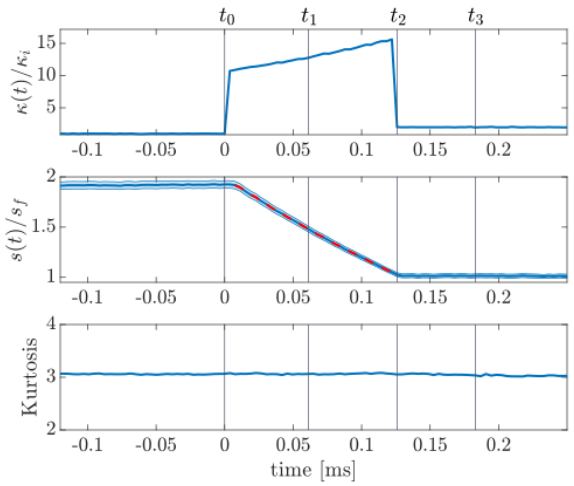

FIG. 6. Top panel: Single cycle of the control parameter $\kappa(t)$ normalized to κ_i for the shortest duration $\Delta t = 1.22 \times 10^{-4}$s protocol. Middle panel: Corresponding time-evolution of the ensemble variance $s(t)$ extracted from the PDF of the ensemble of trajectories, normalized to s_f. The red dashed line, superimposed to $s(t)$ between the transition points, corresponds to the variance extracted from the slopes of the quantile-quantile plots extracted throughout the protocol and shown in the inset of Fig. 8. Bottom panel: Kurtosis evaluated throughout the protocol. The vertical lines represent the four times chosen for the analysis of normality.

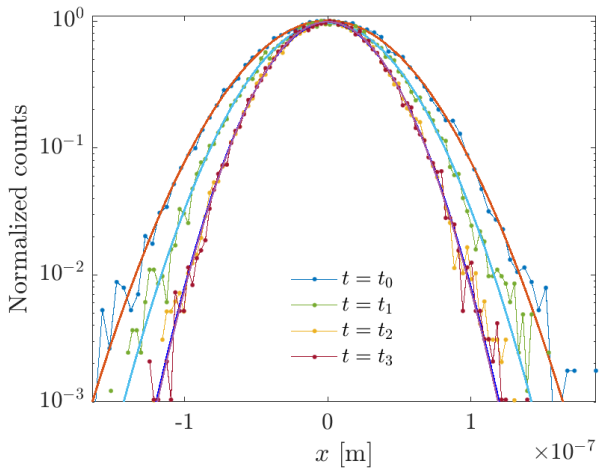

FIG. 7. Normalized PDF represented in log-scale for the four times shown in figure 6. The solid lines represent the results of Gaussian fits.

PSD calibration uncertainties

Under a trapping laser intensity, the registered *p-i-n* voltage values $V(t)$ that correspond to the position fluctuations of the trapped bead are converted into displacement units using the best-fit parameter of the Lorentzian fit of the PSD of the trajectory (at constant κ). The fit parameter D_{fit} is compared to the diffusion coefficient $D = k_B T/\gamma$ expected from the Fluctuation-Dissipation Theorem, assuming known

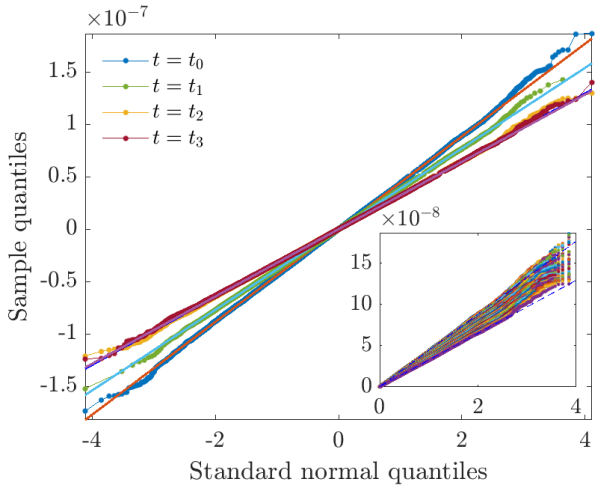

FIG. 8. Quantiles of the PDF at four different times of the protocol as a function of the theoretical quantiles of a standard $\mathcal{N}(0,1)$ normal distribution. The intersection of all curves coincides with the 2-quantile, indicating that all distributions are of zero mean, the slope indicates the variance of the distribution, which, as expected, evolves over time through the protocol. The same analysis is detailed in the inset within the protocol, for times $t_i < t < t_f$. The associated slopes are then superimposed in Fig. 6, middle panel.

temperature and viscosity. This gives a conversion factor $\beta = \sqrt{D/D_{\text{fit}}}$ from *p-i-n* voltages to meters. The uncertainty on the position sensitivity is obtained from standard error propagation including the uncertainty on the viscosity resulting from the $\delta R/R = 2.8\%$ size dispersion deviation of the trapped beads.

Instantaneous positions are thus given from the conversion factor as $x(t) = (\beta \pm \delta\beta)V(t)$, and therefore the variance, up to first-order in uncertainty, $x^2(t) = (\beta^2 \pm 2\beta\delta\beta)V^2(t)$, (since $\mu_x(t) = 0$). The total error of the variance writes as:

$$s(t_j) = \sigma_x^2(t_j) \pm \underbrace{(\delta\sigma_{\chi^2}^2(t_j) + \beta\delta\beta\sigma_x^2(t_j))}_{\delta s(t_j)}, \tag{5}$$

where $\sigma_x^2(t_j) = \sum_{i=1}^{N} |x_i(t_j) - \mu(t_j)|^2/(N-1)$ is the estimator of the instantaneous ensemble variance over N cycles, $\delta\sigma_{\chi^2}^2$ corresponds to the statistical uncertainty in the motional variance determination (see above) and $\delta\beta\sigma_x^2$ the PSD calibration uncertainty just discussed.

The temporal average variances related to the initial an final stiffness s_i and s_f are obtained from temporal average. Assuming Δt as the interval over which $\kappa(t)$ remains constant (either at κ_i or κ_f), the temporal average $\overline{\cdots}$ of the corresponding variance is:

$$\bar{s} = \frac{1}{\Delta t}\sum_{j=1}^{n} s(t_j), \tag{6}$$

taking Δt as the interval over which $\kappa(t)$ remains constant (either at κ_i or κ_f) and $n = \Delta t \cdot f_s$ with $f_s = 262$ kHz, the sampling

frequency. The standard deviation of the temporal average is simply evaluated as:

$$\delta_t \bar{s} = \sqrt{\frac{1}{\Delta t}\sum_{j=1}^{n} |s(t_j) - \langle s \rangle_t|^2} \tag{7}$$

The stationary variances s_i and s_f and their uncertainties are thus simply given by:

$$s_{i,f} = \bar{s} \pm \underbrace{\left(\delta_t \bar{s} + \overline{\delta s} + \delta_t \overline{\delta s}\right)}_{\delta_t s_{i,f}}, \tag{8}$$

where $\overline{\delta s} = 1/\Delta t \sum_{j=1}^{n} \delta s(t_j)$.

Energetics uncertainties

The confidence interval of the mean cumulative work are computed taking into account the uncertainties related to both variances and stiffnesses. They are displayed on all energetic figures at a 95% confidence level.

B: COMPARING OPTIMAL, STEP-LIKE AND ESE PROTOCOLS

We compare here three protocols that transfer the bead between two equilibria, going from an initial stiffness κ_i to a final one κ_f with, for all protocols, fixed and identical κ_f, κ_i values given in the main text.

The first protocol consists of a sudden step-like change of the optical trap stiffness – see Fig. 9, green trace. The second protocol is the "engineered swift equilibriation" (ESE) protocol recently proposed and implemented by Martinez, *et al.* [5]. We calculate $\kappa_{\mathrm{ESE}}(t)$ following [5] for a transfer duration of $\Delta t = 3.47 \times 10^{-4}$ s. Over the same transfer duration, we also implement our optimal protocol $\kappa_{\mathrm{opt}}(t)$. All protocols are displayed in Fig. 9.

Fig. 10 gathers the time evolutions of the motional variances associated with each protocol. As expected, the step-like protocol displays the longest equilibration time when compared to the ESE and optimal protocols. From an energetic point of view, the comparison between the two latter protocols, shown in Fig. 11, clearly reveals the non-optimal character of the ESE protocol with a cumulated work expense larger than for the the optimal protocol. This can also be seen in the inset of Fig. 11 where the excess work expended during the ESE protocol lies clearly above the optimal lower bound discussed in the main text.

C: SMOOTH PROTOCOLS

The optimal protocol obtained in this work [Eq. (6) in the main text] was derived using the Lagrangian density

$$L[s, \hat{\kappa}(s)] = \frac{\gamma}{D\gamma - s\,\hat{\kappa}(s)} - \lambda\,\hat{\kappa}(s). \tag{9}$$

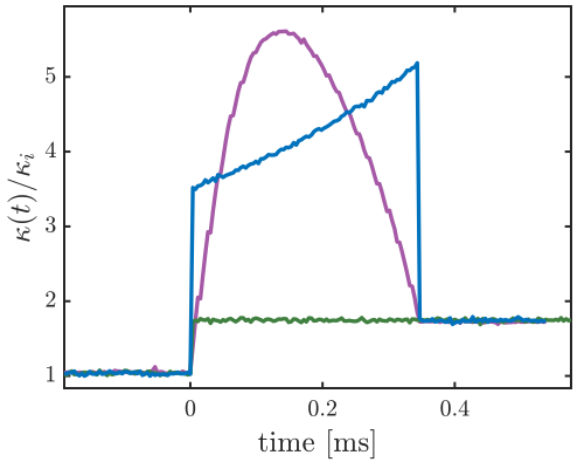

FIG. 9. Calibrated signal of the function generator, for a step-like (green), ESE (pink), and optimal (blue) protocols. The stiffness $\kappa(t)$ is normalized to the initial stiffness κ_i. The jump for the transition $\kappa_i \to \kappa_f$ starts at $t_0 = 0$ s and, for the case of ESE and optimal ends at $\Delta t = 3.47 \times 10^{-4}$ s, with $\kappa_i = 2.77 \pm 0.08, \kappa_f = 5.22 \pm 0.15$ pNμm. The ESE protocol κ_{ESE} was computed based on Eq. (8) in [5].

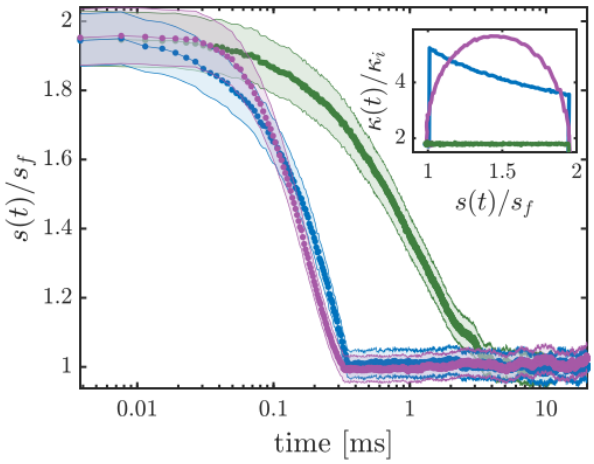

FIG. 10. Temporal evolution of the variance $s(t)$, after $t_0 = 0$ s for the step-like protocol (in green), and the ESE (in purple) and optimal (in blue) protocols. The variances are normalized to the final equilibrated variance s_f. The data points represent ensemble mean values of the variance $s(t)$ for each protocol. The shaded areas show the respective 95% confidence intervals. Both ESE and optimal protocols reach an equilibrium regime s_f at $\Delta t = 3.47 \times 10^{-4}$ s $\sim \tau_{\mathrm{relax}}/10$ by construction. Inset: The control parameter $\hat{\kappa}(s)$ as a function of the variance s, with the same color codes as in the main figure.

A peculiar feature of $L[s, \hat{\kappa}(s)]$ is that the corresponding Euler-Lagrange equation is purely algebraic (as opposed to a differential equation). Hence, it is not possible to impose the desired boundary conditions on the control parameter $\hat{\kappa}(s)$ (i.e. $s_i \kappa_i = s_f \kappa_f = D\gamma$) and two jumps have to be added "by hand" at the beginning and the end of the protocol, as explained in the main text.

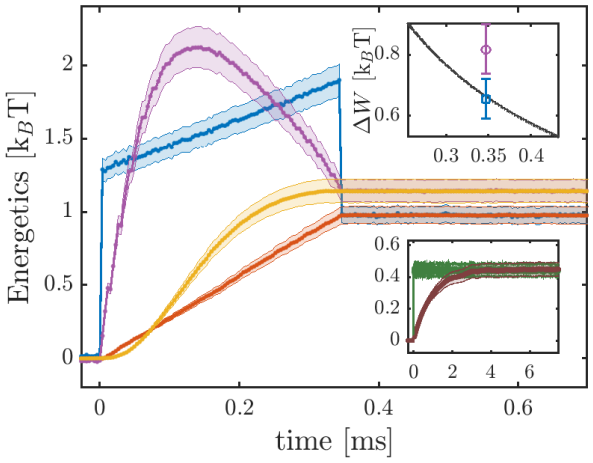

FIG. 11. Temporal evolution of the mean cumulative energetics of the different protocols, step-like (lower inset), ESE and optimal. The mean cumulative work for the optimal protocol is displayed in blue, with total work $W(t)_{\rm opt} = 0.981 \pm 0.059\ k_{\rm B}T$. The mean cumulative work for the ESE protocol is displayed in pink, with total work $W(t)_{\rm ESE} = 1.142 \pm 0.075\ k_{\rm B}T$. The mean cumulative heat generated through the optimal protocol is displayed in orange and the ESE protocol in yellow. Both are superimposed to the work, with total heat $Q(t)_{\rm opt} = 0.983 \pm 0.060\ k_{\rm B}T$ and $Q(t)_{\rm ESE} = 1.142 \pm 0.076\ k_{\rm B}T$. Shaded areas represent 95% confidence levels. Lower inset: Energetics for the step-like protocol. As expected, the mean cumulative work (in green) reaches immediately $W_{\rm step} = 0.45 \pm 0.04\ k_{\rm B}T$. In brown, the heat, in contrast, achieves the equilibrium value $W = Q$ with $Q_{\rm step} = 0.45 \pm 0.04\ k_{\rm B}T$ only after $\tau_{\rm relax}$. Upper inset: Comparison between the excess work values of the ESE protocol (pink) and the optimal one (blue) for the transfer duration of duration $\Delta t = t_f = 3.47 \times 10^{-4}$ s. The non-optimal character of the ESE protocol is directly measured with $\Delta W_{\rm ESE} = 0.81 \pm 0.08\ k_{\rm B}T$ larger than the optimal value $\Delta W_{\rm opt} = 0.65 \pm 0.07\ k_{\rm B}T$. The universal bound $\Delta W = \gamma(\sqrt{s_i} - \sqrt{s_f})^2/\Delta t$ discussed in the main text is shown by the continuous line.

Although these jumps can be realized without much trouble in the experiments, it is interesting to develop a theoretical procedure capable of furnishing a suboptimal protocol $\hat{\kappa}(s)$ that is continuous in the variable s and converges towards the optimal protocol as some parameter tends to zero. To do this, we need to limit the gradient of $\hat{\kappa}(s)$ by adding a further term to the Lagrangian density (9), which becomes:

$$L[s, \hat{\kappa}(s)] = \frac{\gamma}{D\gamma - s\,\hat{\kappa}(s)} - \lambda\,\hat{\kappa}(s) + \varepsilon |\hat{\kappa}'(s)|^2\,, \qquad (10)$$

where ε is an additional Lagrange multiplier. The above Lagrangian density yields the Euler-Lagrange equation:

$$2\varepsilon\,\frac{d^2\hat{\kappa}}{ds^2} = \frac{\gamma s}{(D\gamma - s\hat{\kappa})^2} - \lambda\,. \qquad (11)$$

As a second-order differential equation, Eq. (11) needs two independent boundary conditions, thus enabling us to set $s_i\kappa_i = s_f\kappa_f = D\gamma$, as requested for our protocols. When $\varepsilon \to 0$, we obtain the correct limit case of Eq. (6) in the main text, i.e., the optimal protocol containing two points of infinite derivative (jumps) for the function $\hat{\kappa}(s)$ at s_i and s_f. Through the Lagrange multiplier ε, one can limit the value of such derivative, so that the protocol becomes smoother and smoother as ε increases.

Equation (11) can be solved numerically by successive iterations. We used the following scheme:

$$-\alpha\,\hat{\kappa}_i^{n+1} + 2\varepsilon \left(\frac{d^2\hat{\kappa}}{ds^2}\right)_i^{n+1} = \frac{\gamma s_i}{(D\gamma - s_i\hat{\kappa}_i^n)^2} - \lambda - \alpha\,\hat{\kappa}_i^n\,, \quad (12)$$

where the superscript n denotes the n-th iteration, while the subscript i refers to the discrete grid $s_i = i\,\delta s$, with spacing equal to δs. The second derivative is then approximated with the standard finite-difference formula:

$$\left(\frac{d^2\hat{\kappa}}{ds^2}\right)_i \approx \frac{\hat{\kappa}_{i-1} - 2\hat{\kappa}_i + \hat{\kappa}_{i+1}}{\delta s^2}\,.$$

The parameter $\alpha > 0$ is needed to ensure the convergence of the iterative procedure, but does not affect the final result (indeed it disappears from Eq. (12) when $\hat{\kappa}_i^{n+1} = \hat{\kappa}_i^n$).

As an example, we have solved Eq. (11) with physical parameters $D = \gamma = 1$ and $\lambda = 0.81$, corresponding to a total duration for the optimal protocol $\Delta t_{\rm opt} \sim \tau_{\rm relax}/6$ according to Eq. (8) in the main text. The boundary values are $s_i = 1$ and $s_f = 0.5$, $\kappa_i = 1$ and $\kappa_f = 2$. The smoothness parameter is $\varepsilon = 10^{-5}$. The numerical convergence parameter is set to $\alpha = 0.3$. The result of the numerical integration is given in Figs. 12 and 13, for both the optimal (black lines) and smooth (red lines) protocols. As expected, the smoothed protocol follows closely the optimal one, except near the extremities where it reaches its boundary values smoothly and without jumps. The total time of the smoothed protocol is $0.182 \times \tau_{\rm relax}$, longer than that of the optimal one. But the total work is smaller $W_{\rm smooth} = 1.32 < W_{\rm opt} = 1.38$. The time-energy product is $(\Delta t\,\Delta W)_{\rm smooth} = 0.356 > (\Delta t\,\Delta W)_{\rm opt} = 0.343$, in agreement with the theoretical considerations detailed in the main text.

* giovanni.manfredi@ipcms.unistra.fr
† hervieux@ipcms.unistra.fr
‡ laurent.mertz@nyu.edu
§ genet@unistra.fr

[1] Gabriel Schnoering, Yoseline Rosales-Cabara, Hugo Wendehenne, Antoine Canaguier-Durand, and Cyriaque Genet, "Thermally limited force microscopy on optically trapped single metallic nanoparticles," Phys. Rev. Applied **11**, 034023 (2019).
[2] Gabriel Schnoering, Lisa V. Poulikakos, Yoseline Rosales-Cabara, Antoine Canaguier-Durand, David J. Norris, and Cyriaque Genet, "Three-dimensional enantiomeric recognition of optically trapped single chiral nanoparticles," Phys. Rev. Lett. **121**, 023902 (2018).
[3] A. Manoliu and C. Kittel, "Correlation in the langevin theory of brownian motion," Am. J. Phys. **47**, 678–680 (1979).
[4] Crispin Gardiner, Stochastic Methods (Springer-Verlag, Berlin Heidelberg, 2009).

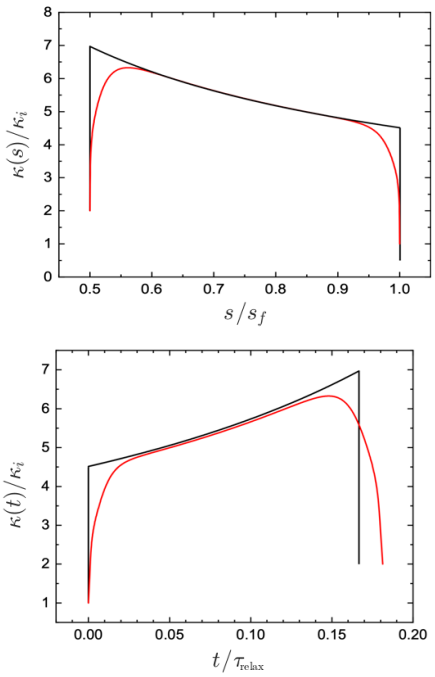

FIG. 12. Smooth protocol obtained from the solution of Eq. (11) (red lines) and corresponding optimal protocol with same value of λ (black lines). Top panel: Protocols in the $(\hat{\kappa}, s)$ plane. Bottom panel: Protocols $\kappa(t)$ as a function of time.

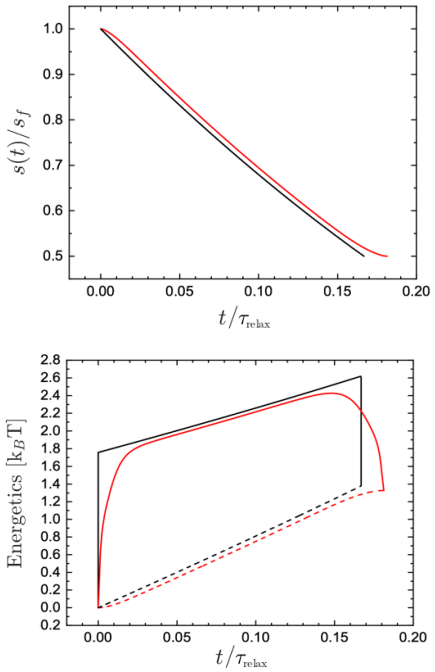

FIG. 13. Smooth protocol obtained from the solution of Eq. (11) (red lines) and corresponding optimal protocol with same value of λ (black lines) . Top panel: Variance $s(t)$ as a function of time. Bottom panel: Dissipated heat $Q(t) = -\frac{1}{2}\int_{t_i}^{t} dt \dot{s}(t)\kappa(t)$ (dashed lines) and expended work $W(t) = \frac{1}{2}\int_{t_i}^{t} dt s(t)\dot{\kappa}(t)$ (solid lines) as a function of time.

[5] Ignacio A. Martínez, Artyom Petrosyan, David Guéry-Odelin, Emmanuel Trizac, and Sergio Ciliberto, "Engineered swift equilibration of a brownian-particle," Nature Phys. **12**, 843 (2016).